Simultaneous Imaging and Selective Photothermal Therapy through Aptamer-Driven Au Nanosphere Clustering

Zhenping Guan,[†] Taishi Zhang,[†,‡] Hai Zhu,[†] Da Lyu,[∥] Sreelatha Sarangapani,[†] Qing-Hua Xu,*[†,‡,∥] and Matthew J. Lang*[†,§]

[†]BioSyM IRG, Singapore−MIT Alliance for Research and Technology, Singapore 138602
[‡]NUS Graduate School for Integrative Sciences & Engineering, Singapore 117456
[§]Department of Chemical and Biomolecular Engineering and Department of Molecular Physiology and Biophysics, Vanderbilt University, Nashville, Tennessee 37235, United States
[∥]Department of Chemistry, National University of Singapore, 3 Science Drive 3, Singapore 117543

S Supporting Information

ABSTRACT: Gold (Au) nanoparticles display enhanced near-infrared (NIR) photo-thermal effects upon the formation of clusters. We studied the photothermal properties of Au nanosphere clusters on the single-particle level using photothermal heterodyne imaging (PTHI) microscopy to understand the enhancement mechanisms. NIR photothermal responses of Au nanoparticle clusters were found to significantly increase from monomers to trimers. The averaged PTHI signal intensity of Au nanosphere dimers and trimers is ∼10 and ∼25 times that of monomers. The NIR photothermal effect of clustered nanospheres strongly correlates with their longitudinal plasmon mode. Clustered Au nanospheres were demonstrated to exhibit dual-capability NIR photo-thermal imaging and therapy of human prostate cancer cells with high efficiency and selectivity. This strategy can be potentially utilized for simultaneous cancer imaging and therapy with 3D selectivity.
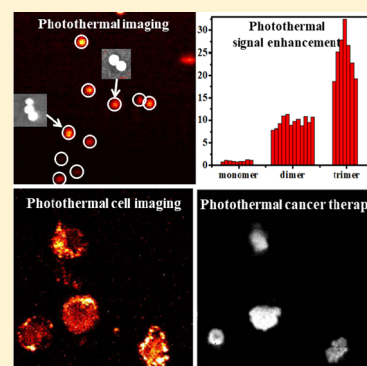
Photothermal therapy is a minimally invasive treatment method where agents absorb and convert photon radiation energy into heat to kill diseased cells of interest.[1−4] Gold nanoparticles (Au NPs) are known as excellent photothermal agents due to their unique physicochemical properties such as chemical inertness, easy functionalization, and, most importantly, localized surface plasmon resonance (SPR).[5] SPR arises from the collective oscillation of free electrons in the conduction band of Au NPs induced by incident radiation. Au NPs show strong light absorption at their SPR frequency and high photon-to-heat conversion efficiencies (>99%), giving rise to excellent photothermal effects.[2,6,7] When performing in vivo photothermal therapy using Au NPs, it is crucial to tune the SPR to the near-infrared (NIR) region where tissue transmissivity is optimal. The SPR wavelength of Au NPs can be tuned by controlling the particle size, shape, and surrounding environment.[8−12] Various immune-targeted Au NPs with NIR SPR have been employed, such as nanorods, nanobranches, and nanoshells.[6,13,14] However, all of these agents suffer from strong photothermal background from collateral untargeted NPs, which are inevitable in real clinical therapy scenarios. Au nanosphere (NS) clusters serve as an appealing background-free alternative. Even though discrete Au NSs are known as poor NIR light absorbers, their clusters are reported to show enhanced NIR absorption, induced by plasmon coupling.[15,16] Plasmon coupling arises when the interparticle separation is

smaller than their size, resulting in red-shifted SPR wavelength and strongly confined local electric fields in between closely spaced Au NPs.[17,18] By using receptor−ligand interactions, surface-modified Au NSs can be clustered on the membranes of target cells, enabling an accurately targeted photothermal therapy effect. Previous studies showed that cells can be killed 10 times more effectively when Au NPs are attached to the cell membrane.[19]

Cells targeted with Au NS clusters are generally difficult to visualize during the real-time therapy process owing to the poor emission yield of Au NPs.[20] Instead of detecting photoluminescence, dark-field scattering of Au NPs has been utilized to detect the targeted cells.[6,21] Nevertheless, as a wide-field microscopy approach, dark-field microscopy lacks the capability of Z sectioning for imaging. It is therefore appealing to develop a background-free technique to simultaneously visualize and kill the cells of interest with 3D sectioning capability.

Although isolated Au NSs are generally known as poor photon emitters, their clusters were reported to show strong two-photon photoluminescence (2PPL) and second-harmonic generation (SHG).[22,23] 2PPL- and SHG-based techniques have been widely utilized in various biological applications with

advantages of high 3D spatial resolution and deep tissue penetration.[24−26] Because discrete Au NSs show weak 2PPL and SHG signals, enhanced 2PPL and SHG of the nanoparticle clusters have been employed as background-free probes for cell imaging.[27,28] However, 2PPL- and SHG-based techniques require the use of high-cost femtosecond lasers, limiting their potential applications.

Here we report a low-cost alternative method employing photothermal heterodyne imaging (PTHI) microscopy. As an absorption-based imaging technique, PTHI uses nonfluorescent probes such as plasmonic nanomaterials as the contrast agent.[29] Our home-built PTHI microscope consists of two tightly focused collinear continuous-wave NIR lasers. A modulated laser beam at 750 nm acted as the heating beam, which was absorbed by the Au NP clusters to result in heat release and local change of refractive index. The probe beam at 850 nm will be modified by the local refractive index change at the same frequency, generating the PTHI signal. Enhanced NIR photothermal responses in the Au NS clusters were demonstrated at both the ensemble and single-particle levels. Immunotargeted Au NSs were then selectively attached onto the membrane of human prostate cancer cells and formed nanoparticle clusters, giving rise to enhanced NIR photothermal therapy effects and improved PTHI signals for PTHI imaging. These aptamer-modified Au NSs also displayed high selectivity toward cancer cells. Because of the use of an NIR continuous-wave laser source, this strategy offers a low-cost alternative for potential applications in simultaneous cancer imaging and therapy with high tissue penetration and 3D imaging capability.

Citrate-capped Au NSs with a diameter of 70 nm were prepared by following a previously reported kinetically controlled seeded growth strategy.[30] The detailed preparation procedure are described in the Supporting Information. The prepared Au NSs are uniform in size and shape with an average diameter of 70 nm (TEM in the Figure S1 in the Supporting Information). The citrate-capped Au NSs bear negative charges on the surface, and the addition of positively charged polyelectrolyte, PDDA, will result in the aggregation of NSs due to electrostatic interactions. Upon the addition of PDDA, the solution rapidly changed color from red to blue, indicating the formation of metal NPs clusters. The TEM images indicated the presence of chainlike nanoparticle clusters of different sizes including dimers, trimers, and larger clusters. Plasmon coupling interactions in these nanoparticle clusters were confirmed by their extinction spectra (Figure 1). The addition of PDDA resulted in a decrease in the original SPR band of Au NSs and the appearance of red-shifted broadened band extending to the NIR region. The extinction in the NIR region gradually increased with increasing concentration of PDDA, indicating the formation of nanoparticle clusters with increasing size and length. The change in their sizes upon the addition of different amounts of PDDA has been further confirmed by TEM images and hydrodynamic dynamic light scattering measurements, as shown in Figures S1 and S2.

The extinction spectrum of Au NPs is a sum of scattering and absorption components. However, only the absorption component contributes to the photothermal effect. The change in the absorption of Au NSs clusters in the NIR region was monitored by a dual-beam thermal-lens spectroscopy (TLS) technique. The experimental setup and procedures are described in the Supporting Information (Figure S3). TLS is a pure absorption-based technique in which absorbed photons are converted into heat, causing a local change in the refractive index to the medium surrounding the nanoparticle, the so-called thermal lens effect. The probe beam (850 nm) transiting the thermal lens was focused into a fiber core, which acts as a pinhole to spatially filter the defocused beam induced by the thermal lens. The temperature gradient is proportional to the amount of absorbed photon energy by the samples, which therefore allows us to determine the change of the absorption of Au NPs at the heating wavelength. The Au NS clusters exhibited (Figure 1B) increased photothermal responses at 750 nm as a result of increased degree of coupling. An up to five-fold increase in the TLS signal was observed when 120 μm PDDA was added.

According to our calculation, there are ∼98 Au NSs in the excitation volume (5.76×10^{-15} m^3; see details in the Supporting Information) of our ensemble-based TLS measurements. The observed increased NIR photothermal effect is thus an ensemble-averaged result of Au NS clusters of different sizes including dimers, trimers, and larger aggregates. Studies of photothermal properties of individual Au NS clusters at the single-particle/cluster level will help us to better understand the underlying enhancement mechanism.

PTHI was employed to study the photothermal properties of single Au NSs or their clusters. The detailed experimental procedures are described in the Supporting Information. PTHI shares a similar experimental setup as TLS. Instead of recording an ensemble-averaged change in the signal intensity, an image was reconstructed by scanning the immobilized Au NS clusters. A pattern-matching method was employed to correlate PTHI images of the nanoparticle clusters and their scanning electron microscopy (SEM) images to identify the region with the same distributions of the particles. Each bright spot in PTHI image corresponds to a nanoparticle or cluster in the SEM image. This procedure allows us to establish the correlation between the nanostructures of different NPs/ clusters and their photothermal properties. The photothermal responses of single nanoparticle clusters were quantitatively evaluated by integrating the PTHI pixel intensities of the bright spot of a 0.8 × 0.8 μm square region. The final signal was obtained by subtracting the background from a nearby 0.8 × 0.8 μm region without any nanoparticles. Figure 2 shows the SEM images of various Au NS clusters as well as their corresponding PTHI images under 750 nm circularly polarized laser excitation. Au NS clusters were found to display significantly stronger PTHI signals than those of the isolated particles.
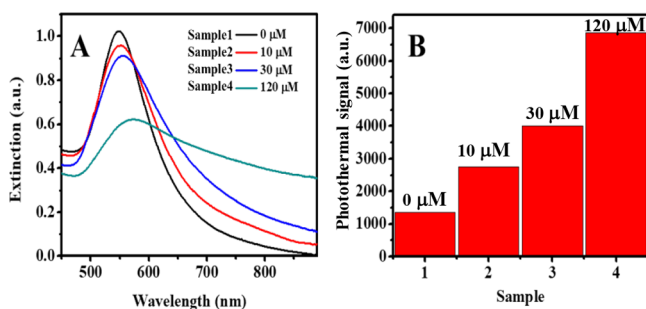

Figure 1. (A) Extinction spectra and (B) photothermal signal of discrete and clustered Au NS solution (in the presence of different amounts of PDDA). The concentration of Au NSs is ∼22.3pM.
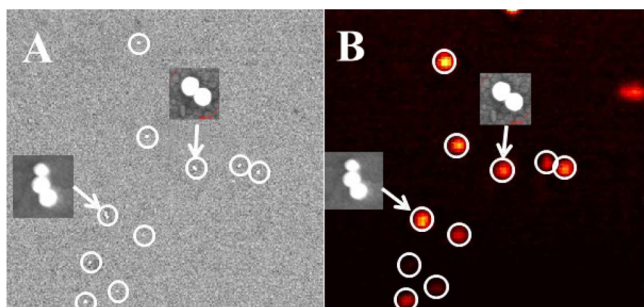
Figure 2. (A) SEM and (B) photothermal heterodyne imaging under 750 nm circular polarization excitation of Au NS clusters.

The correlation between the configuration of various nanoparticle clusters and their photothermal responses was studied by inspection of 9 monomer, 12 dimers, and 7 trimers (Figure 3A). Using the averaged PTHI intensity of 9
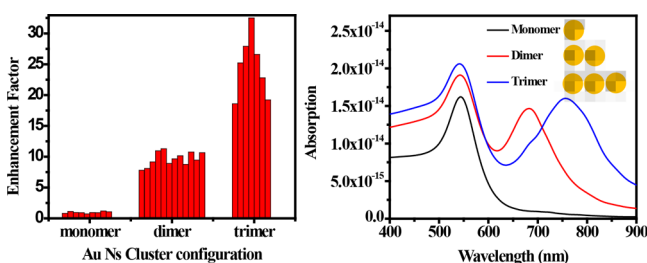

Figure 3. (A) Relative photothermal signals of Au NS monomers, dimers and trimers. (B) Simulated absorption of Au NS monomer, dimer, and linear trimer using finite difference time domain (FDTD) method.

monomers as the reference, the averaged PTHI signal of the dimers and trimers is ~10 and ~25 times that of Au NS monomers, respectively. The variation is due to slight variation in the size of the metal nanoparticles and gap distance between them. The highest enhancement of up to 32.5-fold was obtained for the trimer. Because the PTHI signal is expected to be proportional to the absorption capability of the nanoparticles, enhanced PTHI signals are therefore attributed to increased absorption at the heating laser wavelength. Because it is difficult to measure the absorbance of single particles, finite difference time domain (FDTD) simulations were performed instead to calculate the absorption spectra of single nanoparticle clusters (Figure 3B; the simulation method is described in the Supporting Information). In addition to the fundamental absorption peak at ~540 nm, a new absorption band appears at longer wavelength (peak at ~690 nm) for the dimer, which was further red-shifted to 770 nm for the trimer. On the basis of our simulation results, the absorbance at 750 nm in dimers and trimers was 10.4- and 24.4-fold enhanced, respectively, over that of monomers, which is in excellent consistence with the change in the photothermal signals observed in our experiments. This new peak is a typical feature of the longitudinal plasmon band of coupled metal nanoparticles.[15,31] This new longitudinal band in dimers and linear trimers can be understood in terms of the plasmon hybridization theory.[32−36] When the particles are coupled, their resonance evolved into two orthogonal modes, a red-shifted longitudinal mode and a blue-shifted transverse mode, similar to formation of J-aggregates and H-aggregates of the

molecular excitonic coupling. The formation of the new band gives rise to an increased absorption band in the NIR region.

The observed enhanced NIR photothermal effect is strongly correlated to the longitudinal absorption band in the clusters, which can be further confirmed by the excitation-polarization-dependent PTHI results (Figure 4). The monomer shows
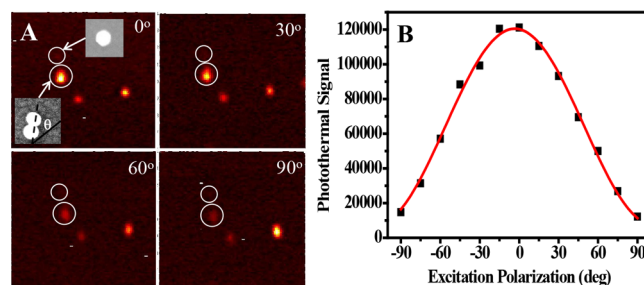

Figure 4. (A) Excitation-polarization-dependent PTHI images. Inset shows the SEM images of the studied Au NS monomer and dimer (circled). (B) Excitation-polarization-dependent photothermal responses of a Au NS dimer.

weak PTHI signals due to its weak absorption at the laser wavelength of 750 nm, which was independent of the excitation polarization. However, the PTHI signal of dimer was strongly dependent on the excitation polarization (Figure 4). Optimum PTHI signal was observed when the excitation polarization was along the long axis ($\theta = 0°$) of the dimer. The PTHI signal gradually deceased when the polarization of the excitation beam changed from parallel ($\theta = 0°$) to perpendicular to the assembly axis ($\theta = 90°$), following a $\cos^2 \theta$ function (Figure 4B). The $\cos^2 \theta$ dependence of the PTHI signal indicates its strong correlation to the longitudinal SPR mode, the coupled nanostructure in the NIR region.

Au NPs have been known to display good biocompatibility and easy surface functionalization. Au NS clusters are expected to act as excellent NIR photothermal agents with dual capability of photothermal cancer cell imaging and therapy. We demonstrated their applications by using the human prostate cancer cell line, LNCaP, as the target, whereas the healthy human prostate epithelial cells (PrECs) were used as the control. The LNCaP cells were reported to overexpress prostate-specific membrane antigen (PSMA) per cell, which is significantly higher than the healthy PrEC cells.[37,38] To specifically target and kill the cancer cells, it is crucial for Au NSs to selectively assemble and form clusters on the membrane of LNCaP cells. This was achieved by modifying the surface of Au NSs with PSMA-specific aptamers, A9 RNA. The successful surface modification has been manifested by the change in its UV−vis extinction and IR spectra of Au NPs before and after aptamer medication (see details in Figure S4). The amount of aptamer on the surface of Au NPs was estimated to be ~6400 per particle by measuring the amount of DNA detached from Au NPs using dithiothreitol (see Figure S5). For direct comparison, the LNCaP and PrEC cells were mixed and cultivated in the same Petri dish. The cells were then incubated with a cell-staining kit (calcein AM and propidium iodide (PI)) and PSMA-modified Au NSs with a concentration of ~10 000 Au NSs per cell. The mixture was directly used in the studies without washing off free unbounded nanoparticles in the medium.

The cell viability was evaluated by fluorescence imaging prior to the photothermal treatment. Calcein AM is a cell-

permeant dye that can only stain the cytoplasm of living cells. Strong green fluorescence was observed from the cells (Figure 5A,D,G), indicating good cell viability. A laser beam at 750 nm
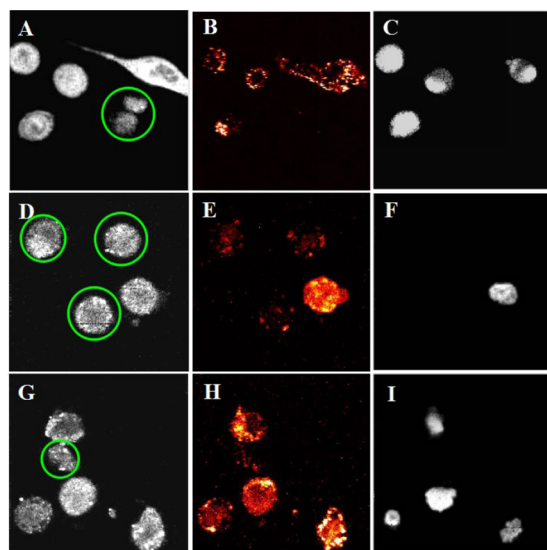

Figure 5. Calcein-AM- (A,D,G) and propidium-iodide- (C,F,I) stained fluorescence scanning imaging and photothermal heterodyne imaging (B,E,H) of the mixed human prostate cancer cells (LNCaP) and normal human prostate epithelial cells (PrECs, in green circles). Image size: 100 × 100 μm.

with power of 2 mW was directed onto the sample plane as the heating source. The polarization of heating beam was adjusted to be circular to excite the nanoparticle clusters of different assembly angles. Another laser beam at 850 nm with power of 2 mW was employed as the probe beam for PTHI imaging. The overall laser power density was calculated to be 1.06 MW·cm^{-2} in the focal area. The photothermal therapy was performed by scanning a 100 × 100 μm area with 0.2 μm pixel size and 3 ms exposure time at each pixel. The PTHI image could be simultaneously recorded. As depicted in Figure 5B,E,H, PTHI images with high contrast were obtained, denoting the formation of the NS clusters. The PTHI images show weak background signals from the free isolated Au NSs in the solution. Figure 5 shows that only the cancer cells give strong PTHI signals, whereas the living PrEC cells (green circles) cannot be visualized in the PTHI images. The capability of selectively imaging cancer cells over healthy cells can be ascribed to fewer PSMA receptor targets on the PrEC membrane, which results in fewer aptamer-modified Au NSs bound to the healthy cell and consequently low PTHI signals. The specific cancer-cell-targeting capability was also evidenced by performing the PTHI imaging experiment on the sample containing PrEC cells only under the same conditions, in which no PTHI signal was observed (Figure S6).

The photothermal therapy effect was evaluated by using a red fluorescent cell-staining dye, PI, which is a DNA intercalator and stains the nucleus of deceased cells only. As shown in Figure 5C,F,I, all of the cells showing strong PTHI signals were killed after the scanning. In contrast, the normal prostate cells PrEC still remained alive. These results indicate good photothermal therapy efficiency and high selectivity of these aptamer-modified Au NSs toward the cancer cells. By using the NIR PTHI microscopy, the Au NS-targeted cancer cells could be simultaneously imaged/detected with high

contrast and selectively killed with high efficiency. The use of NIR light allows deep penetration imaging and therapy treatment due to its coincidence with the biological transparency window in this wavelength range. Similar to two-photon excitation techniques,[39−42] PTHI signal is proportional to the product of the laser intensity of two NIR beams, which enables 3D optical sectioning capability with deep tissue penetration.[43]

In summary, we have successfully demonstrated a new strategy of real-time photothermal therapy and imaging with human prostate cancer cells. The strategy is based on the significantly enhanced photothermal effect of Au NSs upon the formation of clusters. Aptamer-modified Au NSs preferentially target and aggregate onto the membrane of cancer cells. By using PTHI microscopy, the cancer cells can be selectively detected and killed with high efficiency. Because of the high tissue penetration and 3D sectioning of the NIR PTHI microscopy, this strategy can be potentially utilized for simultaneous cancer imaging and therapy.

■ ASSOCIATED CONTENT

Ⓢ Supporting Information

The Supporting Information is available free of charge on the ACS Publications website at DOI: 10.1021/acs.jp-clett.8b03284.

> Sample preparations, experimental procedures, details of material characterizations (TEM, dynamic light scattering, UV−vis extinction, and IR spectra), simulation method, and other supporting data (PDF)

■ AUTHOR INFORMATION

Corresponding Authors
*E-mail: matt.lang@Vanderbilt.Edu (M.J.L.).
*E-mail: chmxqh@nus.edu.sg (Q.-H.X.).

ORCID Ⓘ
Hai Zhu: 0000-0003-3015-7183
Qing-Hua Xu: 0000-0002-4153-0767

Author Contributions
The manuscript was written through contributions of all authors. All authors have given approval to the final version of the manuscript.

Notes
The authors declare no competing financial interest.

■ ACKNOWLEDGMENTS

■ REFERENCES

(1) Yang, K.; Hu, L.; Ma, X.; Ye, S.; Cheng, L.; Shi, X.; Li, C.; Li, Y.; Liu, Z. Multimodal Imaging Guided Photothermal Therapy using Functionalized Graphene Nanosheets Anchored with Magnetic Nanoparticles. *Adv. Mater.* **2012**, *24* (14), 1868−1872.
(2) El-Sayed, I. H.; Huang, X.; El-Sayed, M. A. Selective laser photo-thermal therapy of epithelial carcinoma using anti-EGFR antibody conjugated gold nanoparticles. *Cancer Lett.* **2006**, *239* (1), 129−135.

(3) Moon, H. K.; Lee, S. H.; Choi, H. C. In Vivo Near-Infrared Mediated Tumor Destruction by Photothermal Effect of Carbon Nanotubes. *ACS Nano* **2009**, *3* (11), 3707−3713.

(4) Li, D.; Han, D.; Qu, S.-N.; Liu, L.; Jing, P.-T.; Zhou, D.; Ji, W.-Y.; Wang, X.-Y.; Zhang, T.-F.; Shen, D.-Z. Supra-(carbon nanodots) with a strong visible to near-infrared absorption band and efficient photothermal conversion. *Light: Sci. Appl.* **2016**, *5* (7), No. e16120.

(5) Ehrenreich, H.; Philipp, H. R. Optical Properties of Ag and Cu. *Phys. Rev.* **1962**, *128* (4), 1622−1629.

(6) Huang, X.; El-Sayed, I. H.; Qian, W.; El-Sayed, M. A. Cancer Cell Imaging and Photothermal Therapy in the Near-Infrared Region by Using Gold Nanorods. *J. Am. Chem. Soc.* **2006**, *128* (6), 2115−2120.

(7) Ghosh, P.; Han, G.; De, M.; Kim, C. K.; Rotello, V. M. Gold nanoparticles in delivery applications. *Adv. Drug Delivery Rev.* **2008**, *60* (11), 1307−1315.

(8) Zhao, J.; Pinchuk, A. O.; McMahon, J. M.; Li, S.; Ausman, L. K.; Atkinson, A. L.; Schatz, G. C. Methods for Describing the Electromagnetic Properties of Silver and Gold Nanoparticles. *Acc. Chem. Res.* **2008**, *41* (12), 1710−1720.

(9) Kelly, K. L.; Coronado, E.; Zhao, L. L.; Schatz, G. C. The Optical Properties of Metal Nanoparticles: The Influence of Size, Shape, and Dielectric Environment. *J. Phys. Chem. B* **2003**, *107* (3), 668−677.

(10) Noguez, C. Surface Plasmons on Metal Nanoparticles: The Influence of Shape and Physical Environment. *J. Phys. Chem. C* **2007**, *111* (10), 3806−3819.

(11) Jain, P. K.; Lee, K. S.; El-Sayed, I. H.; El-Sayed, M. A. Calculated Absorption and Scattering Properties of Gold Nanoparticles of Different Size, Shape, and Composition: Applications in Biological Imaging and Biomedicine. *J. Phys. Chem. B* **2006**, *110* (14), 7238−7248.

(12) Zhu, H.; Garai, M.; Chen, Z.; Xu, Q.-H. Two-Photon Excitation of Gold Nanorods Interrupted by Extremely Fast Solvent-to-Metal Electron Transfer. *J. Phys. Chem. C* **2017**, *121* (51), 28546−28555.

(13) Yuan, H.; Khoury, C. G.; Wilson, C. M.; Grant, G. A.; Bennett, A. J.; Vo-Dinh, T. In vivo particle tracking and photothermal ablation using plasmon-resonant gold nanostars. *Nanomedicine* **2012**, *8* (8), 1355−1363.

(14) Huang, X.; El-Sayed, M. A. Gold nanoparticles: Optical properties and implementations in cancer diagnosis and photothermal therapy. *J. Adv. Res.* **2010**, *1* (1), 13−28.

(15) Guan, Z.; Gao, N.; Jiang, X.-F.; Yuan, P.; Han, F.; Xu, Q.-H. Huge Enhancement in Two-Photon Photoluminescence of Au Nanoparticle Clusters Revealed by Single-Particle Spectroscopy. *J. Am. Chem. Soc.* **2013**, *135* (19), 7272−7277.

(16) Lin, S.; Li, M.; Dujardin, E.; Girard, C.; Mann, S. One-Dimensional Plasmon Coupling by Facile Self-Assembly of Gold Nanoparticles into Branched Chain Networks. *Adv. Mater.* **2005**, *17* (21), 2553−2559.

(17) Sonnichsen, C.; Reinhard, B. M.; Liphardt, J.; Alivisatos, A. P. A molecular ruler based on plasmon coupling of single gold and silver nanoparticles. *Nat. Biotechnol.* **2005**, *23* (6), 741−745.

(18) Krenn, J. R.; Dereux, A.; Weeber, J. C.; Bourillot, E.; Lacroute, Y.; Goudonnet, J. P.; Schider, G.; Gotschy, W.; Leitner, A.; Aussenegg, F. R.; Girard, C. Squeezing the Optical Near-Field Zone by Plasmon Coupling of Metallic Nanoparticles. *Phys. Rev. Lett.* **1999**, *82* (12), 2590−2593.

(19) Tong, L.; Zhao, Y.; Huff, T. B.; Hansen, M. N.; Wei, A.; Cheng, J. X. Gold Nanorods Mediate Tumor Cell Death by Compromising Membrane Integrity. *Adv. Mater.* **2007**, *19* (20), 3136−3141.

(20) Dulkeith, E.; Niedereichholz, T.; Klar, T. A.; Feldmann, J.; von Plessen, G.; Gittins, D. I.; Mayya, K. S.; Caruso, F. Plasmon emission in photoexcited gold nanoparticles. *Phys. Rev. B: Condens. Matter Mater. Phys.* **2004**, *70* (20), 205424.

(21) Qian, W.; Huang, X.; Kang, B.; El-Sayed, M. A. Dark-field light scattering imaging of living cancer cell component from birth through division using bioconjugated gold nanoprobes. *J. Biomed. Opt.* **2010**, *15* (4), 046025−046025−9.

(22) Ueno, K.; Juodkazis, S.; Mizeikis, V.; Sasaki, K.; Misawa, H. Clusters of Closely Spaced Gold Nanoparticles as a Source of Two-Photon Photoluminescence at Visible Wavelengths. *Adv. Mater.* **2008**, *20* (1), 26−30.

(23) Butet, J.; Brevet, P.-F.; Martin, O. J. F. Optical Second Harmonic Generation in Plasmonic Nanostructures: From Fundamental Principles to Advanced Applications. *ACS Nano* **2015**, *9* (11), 10545−10562.

(24) Helmchen, F.; Denk, W. Deep tissue two-photon microscopy. *Nat. Methods* **2005**, *2* (12), 932−940.

(25) Brown, E.; McKee, T.; diTomaso, E.; Pluen, A.; Seed, B.; Boucher, Y.; Jain, R. K. Dynamic imaging of collagen and its modulation in tumors in vivo using second-harmonic generation. *Nat. Med.* **2003**, *9* (6), 796−800.

(26) Zoumi, A.; Yeh, A.; Tromberg, B. J. Imaging cells and extracellular matrix in vivo by using second-harmonic generation and two-photon excited fluorescence. *Proc. Natl. Acad. Sci. U. S. A.* **2002**, *99* (17), 11014−11019.

(27) Yuan, P.; Ding, X.; Guan, Z.; Gao, N.; Ma, R.; Jiang, X.-F.; Yang, Y. Y.; Xu, Q.-H. Plasmon-Coupled Gold Nanospheres for Two-Photon Imaging and Photoantibacterial Activity. *Adv. Healthcare Mater.* **2015**, *4* (5), 674−678.

(28) Demeritte, T.; Fan, Z.; Sinha, S. S.; Duan, J.; Pachter, R.; Ray, P. C. Gold Nanocage Assemblies for Selective Second Harmonic Generation Imaging of Cancer Cell. *Chem. - Eur. J.* **2014**, *20* (4), 1017−1022.

(29) Boyer, D.; Tamarat, P.; Maali, A.; Lounis, B.; Orrit, M. Photothermal Imaging of Nanometer-Sized Metal Particles Among Scatterers. *Science* **2002**, *297* (5584), 1160−1163.

(30) Han, F.; Guan, Z.; Tan, T. S.; Xu, Q.-H. Size-Dependent Two-Photon Excitation Photoluminescence Enhancement in Coupled Noble-Metal Nanoparticles. *ACS Appl. Mater. Interfaces* **2012**, *4* (9), 4746−4751.

(31) Jiang, X.-F.; Pan, Y.; Jiang, C.; Zhao, T.; Yuan, P.; Venkatesan, T.; Xu, Q.-H. Excitation nature of two-photon photoluminescence of gold nanorods and coupled gold nanoparticles studied by two-pulse emission modulation spectroscopy. *J. Phys. Chem. Lett.* **2013**, *4* (10), 1634−1638.

(32) Yang, S.-C.; Kobori, H.; He, C.-L.; Lin, M.-H.; Chen, H.-Y.; Li, C.; Kanehara, M.; Teranishi, T.; Gwo, S. Plasmon hybridization in individual gold nanocrystal dimers: direct observation of bright and dark modes. *Nano Lett.* **2010**, *10* (2), 632−637.

(33) Nordlander, P.; Oubre, C.; Prodan, E.; Li, K.; Stockman, M. Plasmon hybridization in nanoparticle dimers. *Nano Lett.* **2004**, *4* (5), 899−903.

(34) Prodan, E.; Radloff, C.; Halas, N. J.; Nordlander, P. A hybridization model for the plasmon response of complex nanostructures. *Science* **2003**, *302* (5644), 419−422.

(35) Brandl, D. W.; Mirin, N. A.; Nordlander, P. Plasmon modes of nanosphere trimers and quadrumers. *J. Phys. Chem. B* **2006**, *110* (25), 12302−12310.

(36) Garai, M.; Zhang, T.; Gao, N.; Zhu, H.; Xu, Q.-H. Single Particle Studies on Two-Photon Photoluminescence of Gold Nanorod−Nanosphere Heterodimers. *J. Phys. Chem. C* **2016**, *120* (21), 11621−11630.

(37) Israeli, R. S.; Powell, C. T.; Corr, J. G.; Fair, W. R.; Heston, W. D. Expression of the prostate-specific membrane antigen. *Cancer Res.* **1994**, *54* (7), 1807−1811.

(38) Pinto, J. T.; Suffoletto, B. P.; Berzin, T. M.; Qiao, C. H.; Lin, S.; Tong, W. P.; May, F.; Mukherjee, B.; Heston, W. Prostate-specific membrane antigen: a novel folate hydrolase in human prostatic carcinoma cells. *Clin. Cancer Res.* **1996**, *2* (9), 1445−1451.

(39) Zhao, T.; Yu, K.; Li, L.; Zhang, T.; Guan, Z.; Gao, N.; Yuan, P.; Li, S.; Yao, S. Q.; Xu, Q.-H.; et al. Gold nanorod enhanced two-photon excitation fluorescence of photosensitizers for two-photon imaging and photodynamic therapy. *ACS Appl. Mater. Interfaces* **2014**, *6* (4), 2700−2708.

(40) Shen, X.; Li, L.; Wu, H.; Yao, S. Q.; Xu, Q.-H. Photosensitizer-doped conjugated polymer nanoparticles for simultaneous two-photon imaging and two-photon photodynamic therapy in living cells. *Nanoscale* **2011**, *3* (12), 5140−5146.

(41) Polavarapu, L.; Manna, M.; Xu, Q.-H. Biocompatible glutathione capped gold clusters as one-and two-photon excitation fluorescence contrast agents for live cells imaging. *Nanoscale* **2011**, *3* (2), 429−434.

(42) Perillo, E. P.; Jarrett, J. W.; Liu, Y.-L.; Hassan, A.; Fernée, D. C.; Goldak, J. R.; Bonteanu, A.; Spence, D. J.; Yeh, H.-C.; Dunn, A. K. Two-color multiphoton in vivo imaging with a femtosecond diamond Raman laser. *Light: Sci. Appl.* **2017**, *6* (11), No. e17095.

(43) Gaiduk, A.; Ruijgrok, P. V.; Yorulmaz, M.; Orrit, M. Detection limits in photothermal microscopy. *Chem. Sci.* **2010**, *1* (3), 343−350.